Summary of Full-Scale Blade Displacement Measurements of the UH-60A Airloads Rotor

Anita I. Abrego
Aerospace Engineer

Larry Meyn
Aerospace Engineer

NASA Ames Research Center
Moffett Field, California

Alpheus W. Burner
Aerospace Engineer
Jacobs Technology
Hampton, Virginia

Danny A. Barrows (Retired)
Aerospace Engineer
NASA Langley Research Center
Hampton, Virginia

ABSTRACT

Blade displacement measurements using multi-camera photogrammetry techniques were acquired for a full-scale UH-60A rotor, tested in the National Full-Scale Aerodynamic Complex 40-Foot by 80-Foot Wind Tunnel. The measurements, acquired over the full rotor azimuth, encompass a range of test conditions that include advance ratios from 0.15 to 1.0, thrust coefficient to rotor solidity ratios from 0.01 to 0.13, and rotor shaft angles from -10.0 to 8.0 degrees. The objective was to measure the blade displacements and deformations of the four rotor blades and provide a benchmark blade displacement database to be utilized in the development and validation of rotorcraft prediction techniques. An overview of the blade displacement measurement methodology, system development, and data analysis techniques are presented. Sample results based on the final set of camera calibrations, data reduction procedures and estimated corrections that account for registration errors due to blade elasticity are shown. Differences in blade root pitch, flap and lag between the previously reported results and the current results are small. However, even small changes in estimated root flap and pitch can lead to significant differences in the blade elasticity values.

NOTATION

c	blade chord, in
C_T	rotor thrust coefficient
C_Q	rotor torque coefficient
C_T/σ	ratio of thrust coefficient to rotor solidity
M_{tip}	blade tip Mach number
r	rotor radial coordinate, in
R	rotor radius, 322 in
X	rotor coordinate system spanwise, in
ΔX	elastic deformation of the blade along the x-axis, in
Y	rotor coordinate system chordwise, in
ΔY	elastic deformation of the blade along the y-axis, in
Z	rotor coordinate system vertical, in
ΔZ	elastic deformation of the blade along the z axis, in
α	shaft angle of attack, positive aft, deg
β	blade flap angle, deg
Δtwist	elastic deformation of the blade about the ¼-chord axis, positive nose up, deg
μ	advance ratio
θ	blade pitch angle, deg
σ	rotor solidity, 0.0826
ζ	blade lag angle, deg
ψ	rotor azimuth, deg (0 aft)

Presented at the 2016 AHS Technical Meeting on Aeromechanics Design for Vertical Lift, Fisherman's Wharf, San Francisco, CA, January 20–22, 2016.

INTRODUCTION

A full-scale wind tunnel test of the UH-60A Airloads rotor was completed in the USAF National Full-Scale Aerodynamics Complex (NFAC) 40- by 80-Foot Wind Tunnel at NASA Ames Research Center in May 2010 (Ref. 1). The test was a joint venture between NASA and the U.S. Army to acquire an expanded database, supplementing the widely used and extensive 1993 UH-60A airloads flight test data (Ref. 2). Unique measurement techniques, such as blade displacement multi-camera photogrammetry, were implemented to expand the airloads database and assist with the validation of rotorcraft predictive tools.

Blade displacement measurements are used to resolve rotor blade shape and position, including blade root pitch, flap, lag and elastic deformations. When combined with blade airloads and wake measurements, a comprehensive dataset is formed that directly relates rotor performance to the physical properties of the flow. The accurate prediction of rotor blade rigid body motion and elastic displacements is

a key goal in the development of improved rotorcraft design and analysis techniques. The availability of detailed experimental measurements obtained under conditions representative of the actual flight environment should lead to improved multi-disciplinary, higher fidelity rotorcraft aeromechanics analysis techniques.

Detailed measurements of rotor blade displacements are relatively rare and traditionally have been measured with strain gauges embedded in the rotor blade. However, due to blade size limitations and the limited availability of rotating instrumentation channels, the number of possible sensors is usually insufficient to fully resolve the blade motion. As an alternative, optical methods can be used to provide a fairly accurate description of the blade geometry over much of its length with the added benefit of reduced fabrication costs and sensor count (Ref. 3). For example, in 2001, stereo pattern recognition was used for the Higher Harmonic Control Aeroacoustic Rotor Test (HART II) to measure blade position and displacement of a 40% Mach scaled, 2-meter radius BO-105 model rotor. The technique used was based on a 3-dimensional reconstruction of visible marker locations using stereo photogrammetry, providing the blade motion parameters in flap, lag and torsion (Ref. 4).

In preparation for the UH-60A Airloads wind tunnel test, rotor blade displacement measurements were acquired during two earlier wind tunnel tests in the NFAC 40- by 80-Foot Wind Tunnel. Limited blade displacement measurements were acquired during the 2008 Smart Material Actuated Rotor Technology (SMART) test and again in 2009, during the Individual Blade Control (IBC) test (Ref. 5-6). This particular wind tunnel schedule, having three back-to-back entries in the same facility, allowed the photogrammetry system to progressively expand with each test. A single PC assembly with two-cameras was used for the SMART test, two PCs with four-cameras were used for the IBC test, and four PCs with eight-cameras were used for the final and more extensive Airloads test. The measurement efforts during the first two test entries significantly influenced and improved the final system design for the more expansive blade displacement measurements during the Airloads test.

This paper presents an overview and an update of the blade displacement methodology and system development used for the Airloads test. Previously reported blade displacement results (Ref. 5-9) are now superseded by the results presented in this paper and comprehensively, in "Volume II – Select Data and Plots," of the final blade displacement report (Ref. 10).

TEST DESCRIPTION

The 2010 Airloads test conducted in the NFAC 40- by 80-Foot Wind Tunnel used a Sikorsky Aircraft UH-60A rotor system mounted on the NASA Large Rotor Test Apparatus (LRTA) as seen in Fig. 1. The closed test section consists of semicircular sides and closed-circuit air return passage that are lined with sound-absorbing material to reduce acoustic reflections. The test section dimensions are 39 feet high, 79 feet wide, and 80 feet long with a maximum test section velocity of approximately 300 knots. The LRTA, a special-purpose drive and support system designed to test helicopters and tilt rotors in the NFAC (Ref. 11), was mounted on three struts, allowing for an angle-of-attack range of +15° to -15°.

Figure 1. UH-60A Airloads rotor installed on the Large Rotor Test Apparatus (LRTA) in the NFAC 40- by 80-Foot Wind Tunnel.

The UH-60A is a four-bladed articulated rotor system consisting of a hub, blade pitch controls, bifilar vibration absorber, and main rotor blades. The blades used in this wind tunnel test were the same four rotor blades flown during the UH-60A Airloads Program (Ref. 2). Two blades were heavily instrumented, one with 242 dynamic pressure transducers (blade 1) and the other with a mix of strain-gages and accelerometers (blade 3). A summary of the rotor system parameters is provided in Table 1.

Table 1. UH-60A Rotor Parameters (Ref. 7).

Parameter	Value
Number of blades	4
Radius, in	322
Nominal chord, in	20.76
Equivalent blade twist, deg	-18
Blade tip sweep, deg aft	20
Geometric solidity ratio	0.0826
Airfoil section designation	SC1095/SC1094R8
Thickness, % chord	9.5
100% RPM	258

Although the UH-60A is classified as an articulated or hinged helicopter, there are no actual hinges at the blade root. Rather, the blade motions occur around elastomeric bearings and the "hinges" are the focal points of the bearings. During both the flight and wind tunnel tests, measurements of the blade motions about these focal points were accomplished through a combination of Rotary Variable Differential Transformers (RVDTs) and links, referred to as the Blade Motion Hardware (BMH) or "crab

arm" (Ref. 1). A crab arm is installed on each blade and provides measurements of the blade root flap, lead-lag, and pitch angles.

A second blade motion measurement system composed of four sets of three laser distance transducers (one set mounted to each hub arm) as described in Ref. 1, was also used. The calibration of both systems was performed simultaneously in the wind tunnel.

Test Conditions

The primary wind tunnel test data were acquired during speed sweeps at 1-g simulated flight conditions up to an advance ratio of $\mu = 0.4$, and during parametric thrust sweeps (up to and including stall) at various combinations of shaft angles and forward speeds. Data were also acquired at conditions matching previous full-scale flight test, small-scale wind tunnel tests and while performing unique slowed-rotor simulations at reduced RPM (40% and 65%), up to an advance ratio of $\mu = 1.0$. Detailed descriptions of these test conditions are presented in Reference 1. A summary of the wind tunnel test conditions can be found in the Appendix.

GEOMETRY

Three coordinate systems are used in the analysis of the Airloads photogrammetry data. These three systems are the wind tunnel coordinate system, the rotor hub coordinate system and the rotor blade coordinate system. The photogrammetry system measures all target locations in the wind tunnel coordinate system. Targets located on the test section ceiling are used in the wind tunnel coordinate system for calibration of camera locations, pointing angles, and distortion coefficients. However, targets on the rotor hub and blades need to be transformed to the rotor hub and rotor blade coordinate systems respectively.

Wind Tunnel Coordinate System

Photogrammetric measurements were made in the wind tunnel coordinate system, which is depicted schematically in Fig. 2. The origin of the wind tunnel coordinate system is directly above the turntable center at the stream-wise test section centerline. The x-axis is positive downstream, the z-axis is positive in the vertical direction and the y-axis, defined by the right-hand rule, is positive in the starboard direction. The center of the UH-60A rotor hub at 0° angle-of-attack is located directly over the wind tunnel's main support struts, approximately 85.9 inches upstream of the turntable center.

Rotor Hub Coordinate System

The rotor hub coordinate system is aligned with the LRTA body axis. The LRTA is not perfectly aligned with the test section centerline, but has a slight angular offset of 0.23° toward the starboard as shown in Fig. 3. Important hub and LRTA reference points with respect to the hub moment center is illustrated in a profile view of the UH-60A rotor hub and the LRTA in the 40- by 80- Foot Wind Tunnel test section (Fig. 4). The ball socket centerline is the location about which the model is rotated to set angle-of-attack, α. As shown, the hub moment center is 243.48 inches above the surface of the acoustic floor. The surface of the acoustic floor is 234 inches below the test section centerline (20 feet minus the 6 inch depth of the acoustic floor). These dimensions were used to determine the Z-axis locations of the UH-60A/LRTA reference locations presented in Table 2.

Rotor blade positions and orientations are referenced to the center and plane of rotation of the hub. When the LRTA is at a non-zero angle-of-attack, the hub center and its plane of rotation are rotated about the ball socket depicted in Fig. 4, which results in a rotation and translation of the hub coordinate system that is used for rotor blade positions and orientations.

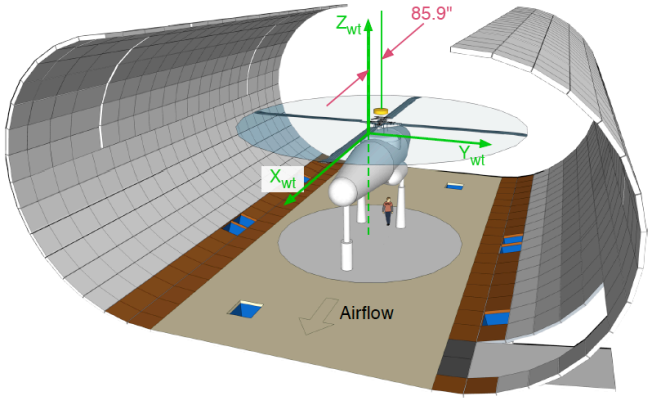

Figure 2. Orientation of the UH-60A/LRTA in the 40- by 80- Foot Wind Tunnel test section coordinate system.

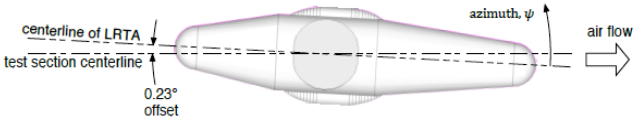

Figure 3. Overhead view of the LRTA alignment with the 40- by 80- Foot Wind Tunnel test section centerline.

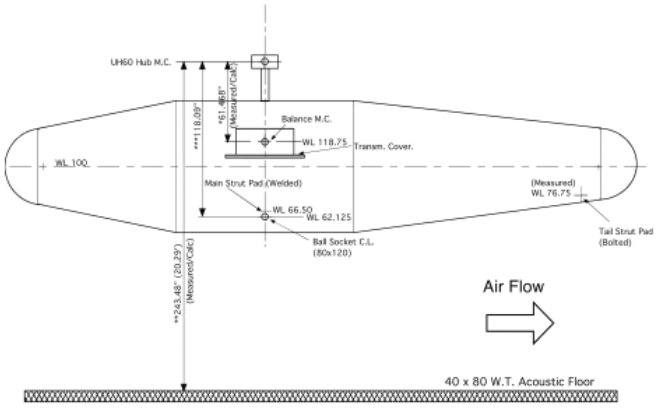

Figure 4. Profile view of the UH-60A rotor hub and the LRTA in the 40- by 80- Foot Wind Tunnel test section.

Table 2. UH-60A/LRTA reference locations in the wind tunnel coordinate system (α = 0 deg).

	X (in)	Y (in)	Z (in)
Rotor Hub Center	-85.9	0	9.48
Angle-of-Attack Pivot Point	-85.9	0	-108.61
Balance Moment Center	-85.9	0	-51.988

Rotor Blade Coordinate System

The UH-60A has four rotor blades numbered 1 through 4 as shown in Fig. 5. The rotor hub/shaft rotation angle about the shaft, or shaft azimuth, ψ, is defined as zero when the principal quarter-chord line of blade 1, at zero lag angle, is aligned with the aft centerline of the LRTA. The UH-60A rotor blade has a complex shape where the airfoil profile, twist and sweep all vary along the span. Pitch, flap, lag and elastic deformations can be thought of as being applied to a rectangular prism or bounding box that encompasses the blade in 3-D space. Figure 6 shows an end view of this bounding box with a selection of the UH-60A airfoil profiles from different radial stations.

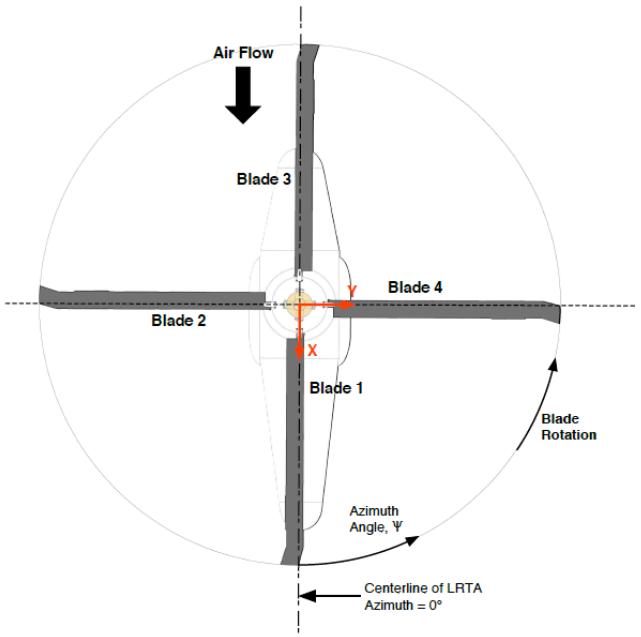

Figure 5. Top-view schematic of the test installation. All blades are shown with zero lag. The quarter-chord line of Blade 1 is aligned with the downstream LRTA centerline, which defines the zero azimuth position for the rotor hub and shaft.

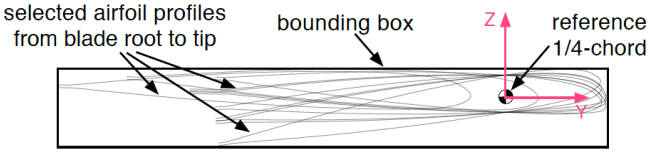

Figure 6. End view of the bounding box encompassing the UH-60A rotor blade.

Blade position and orientation is defined by four rigid body rotation angles applied with respect to the reference orientation of each blade at 0° azimuth. These four angles, in the order of application, are pitch, θ, flap, β, lag, ζ and azimuth, ψ. A simplified representation of the rotor blade rotation angles is shown in Figure 7. Pitch, θ, is the first rotation angle applied to the reference geometry of the blade (Fig. 7a). The pitch angle is where the blade is rotated in the vertical yz plane about its feathering axis, which is coincident with the x-axis of the hub coordinate system. Second, the blade is rotated in the vertical xz plane about its hinge point by the flap angle, β, as shown in Fig. 7b. Third, a horizontal rotation about the hinge point by the lag angle, ζ, is applied to the blade (Fig 7c). And finally, the blade and hub are rotated together in the hub rotation plane about the hub center by the blade azimuth angle, ψ, also shown in Fig. 7c.

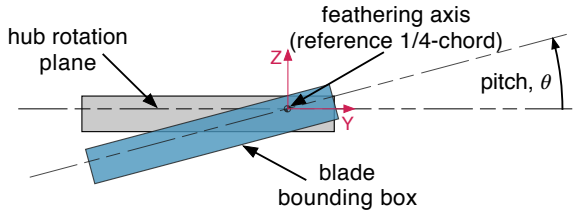

a. Pitch angle, θ, where the blade (end view) is rotated in the yz plane about its reference quarter-chord.

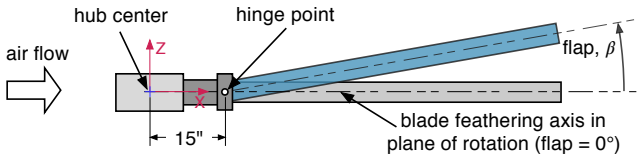

b. Flap angle, β, where the blade is rotated in the vertical xz plane about its hinge point.

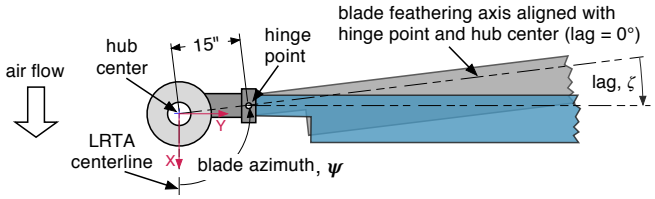

c. Lag angle, ζ, where the blade is rotated horizontally about the hinge point. And blade azimuth, ψ, where the blade and hub are rotated together in the about the hub center.

Figure 7. Rotor blade rotation angles.

Elastic Blade Deformation Geometry

Elastic blade deformation variables represent the subtraction, in the blade reference coordinate system, of rigid blade geometry from the measured, elastically deformed blade geometry. These variables, Δx, Δy, Δz, and Δtwist, are defined for the locations along the feathering axis as shown in Fig. 8. It is assumed that the rigid blade and the

elastically deformed blade have the same pitch, flap, lag and azimuth orientation at the blade root. Errors in the estimated blade root orientation propagate into errors in the elastic deformation variables.

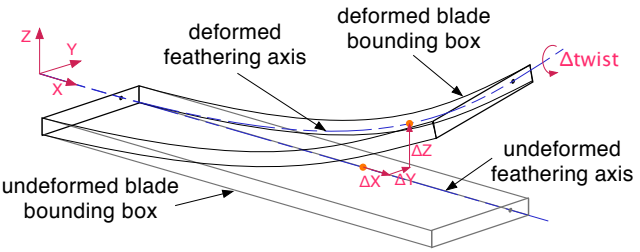

Figure 8. Rotor blade deformation variable definitions.

BLADE DISPLACEMENT SYSTEM

The blade displacement (BD) experimental technique is based on the principles of digital close-range photogrammetry (Ref. 12). The optical method of photogrammetry has been used in a number of wind tunnels to measure aeroelastic deformations (Ref. 13-14). During the Airloads test, multiple cameras were used to determine the spatial coordinates of retro-reflective targets attached to the lower surface of the blade. These coordinates were then used to extract pitch, flap, and lag angles, along with elastic bending and twist for each rotor blade. An overview of the test hardware preparation, camera selection, hardware installation and data acquisition system are presented below.

Hardware Preparation

Retro-reflective targets, cut from 4-mil thick, 3M Scotchlite 7610, high reflectance adhesive tape were applied to both the lower surface of the blades and the test section ceiling (Fig. 9a). Eighty-four, six-inch diameter targets, along with 0.5-inch control targets and a small cluster of 0.5-inch diameter coded targets were mounted on plates and installed on the test-section ceiling. The coded and control targets were used to assist with automated target recognition. Additionally, forty-eight 2-inch diameter retro-reflective targets were installed on each blade. The blade targets were three per radial station, uniformly spaced at approximately 0.05R intervals between the blade cuff and blade tip and covered the blade span from approximately r/R = 0.20 to 0.97. Small blade-to-blade variations in target locations were necessary to avoid other surface-mounted blade instrumentation. Figure 9b shows the targets mounted on the lower surface of blade 4. The additional coded targets and reference targets shown in this image were used to aid in the blade target location measurement process. A schematic showing target centroid locations in the blade coordinate system is shown in Fig 9c.

Blade and ceiling target spatial locations were measured using a V-STARS photogrammetry system, developed by Geodetic Systems Inc. (Ref. 15). The standard deviations of the ceiling and the blade target measurements were typically less than 0.04 inch and 0.001 inch, respectfully. Further details of the V-STARS measurements can be found in Ref. 6. The mappings of each blade in an un-deformed state, as measured in a laboratory setting, serve as reference geometries. The measured spatial data for the blades at any azimuth are then transformed to align with the reference geometries aligned at 0° azimuth to determine root pitch, flap, lag, elastic twist, elastic flap bending, elastic lag bending, and radial deformations. For each blade the rigid body motion estimates (determined from the 12 targets at the four inboard radial stations, r/R = 0.20 to 0.35) are used to transform all targets. All available blade targets are then used in the computation of elastic blade deformations.

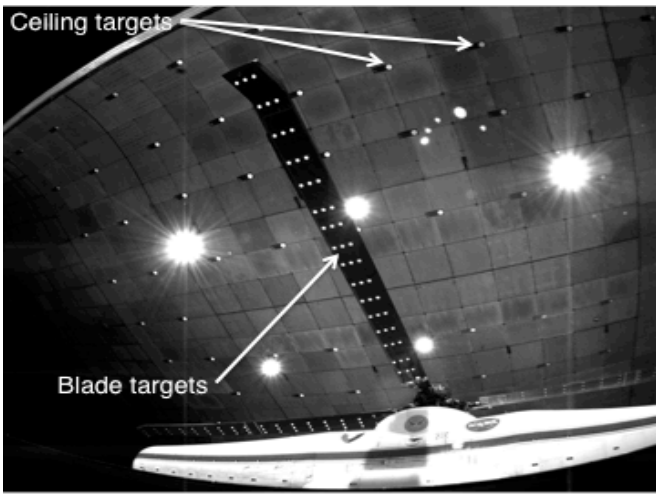

a. Rotor blade and test section ceiling retro-reflective targets.

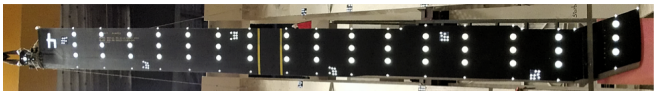

b. Photograph of targets on blade 4.

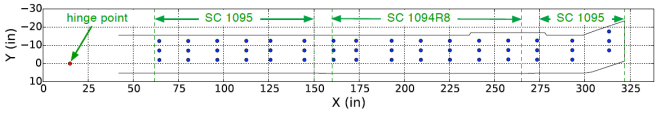

c. Schematic showing the blade lower surface planform with the target locations and the extent of airfoil profile sections.

Figure 9. Rotor blade and test section ceiling retro-reflective targets.

Cameras

The BD system used eight 4-Mega-pixel, 12-bit CCD progressive scan Imperx IPX-4M15-L digital cameras, with a resolution of 2048 × 2048 pixels. To capture the full motion of each rotor blade with at least two cameras, each camera's image field-of-view included a blade azimuth range of at least 90°. The overall translational movement experienced by the rotor blades due to angle-of-attack changes, blade flapping and elastic blade deformations further expanded the lens field-of-view requirements. As a result, in order to encompass this full range of blade motion and the camera installation constraints of the test section,

Nikon 10.5 mm f/2.8 DX (fish-eye) lenses were selected as a compromise. Such short focal length "fish-eye" lenses are not typically used in photogrammetry applications because of the difficulty in obtaining sufficiently accurate distortion corrections. Lens calibrations, mentioned in Reference 6, can partially correct the troubling lens distortions that otherwise reduce the accuracy of the measurements.

Installation

Prior to the start of the UH-60A full-scale wind tunnel test, the BD system setup focused on ensuring high image quality (particularly lighting), optimal orientation angles of the cameras, and adequate coverage on the camera image planes across the complete rotor disk for the anticipated test conditions. A top-view schematic of the LRTA, rotor blades, camera locations and quadrant identifications is illustrated in Fig. 10. The blades, numbered 1 to 4, rotate counter-clockwise when viewed from above. The 0° azimuth location of each blade is defined as aft, over the tail of the LRTA. The four quadrants that make up the rotor disk are designated as Q-I thru Q-IV. Because the rotary shaft encoder 1/rev signal is referenced to blade 1, the azimuth angles of the other three blades must be calculated from the azimuth position of blade 1. The eight BD cameras were positioned such that two cameras predominantly viewed each rotor quadrant. Cameras 1 and 2 view Q-I, cameras 3 and 4 view Q-II, etc. The camera locations were not symmetrical about the rotor shaft due to differences in blade motion on the advancing and retreating side of the rotor, based on experience from the SMART and IBC tests. Figure 11 illustrates the camera viewport locations in the test

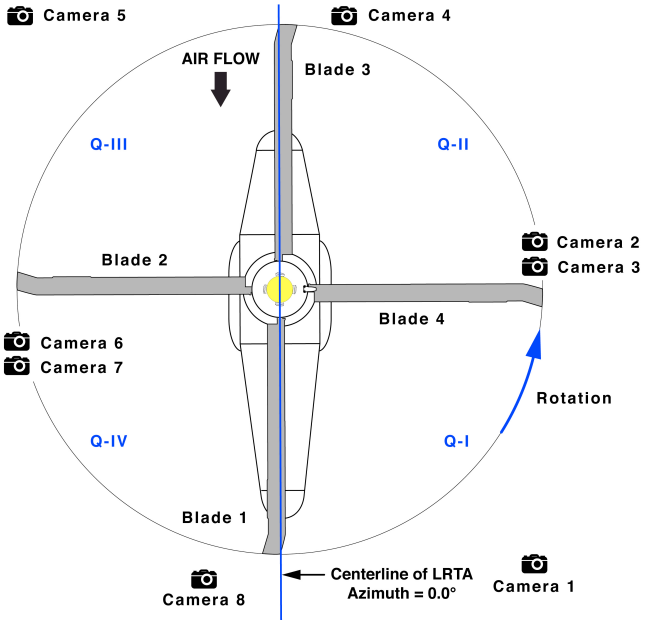

Figure 10. Top-view schematic of the test installation with blade numbers, cameras and rotor quadrants identified.

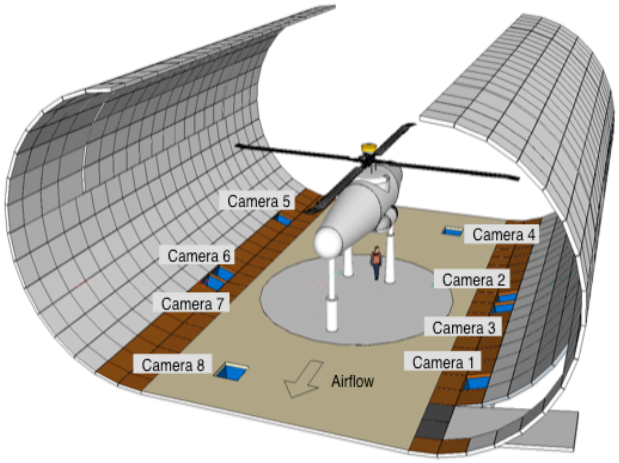

Figure 11. Test section schematic illustrating camera view port locations.

section. Although each camera pair was arranged to view a single rotor quadrant, the view from a given camera was not necessarily limited to that specified quadrant. Therefore, a blade could often be viewed by more than two cameras, resulting in potential multi-camera photogrammetric intersection of the blade targets at many azimuths.

The cameras were securely anchored inside the test section floor camera viewports, facing upward to view the lower surfaces of the blades through protective low-reflectance glass windows (Fig. 12). These low-reflectance windows were procured especially for the UH-60A test to reduce troublesome reflections from the fiber optic bundle illuminators. Target illumination was provided by Perkin-Elmer Machine Vision 7060-10 xenon flash-lamp 50 mJ strobes with pulse duration of 10 microseconds (full width at 1/3 maximum). Fiber optic bundles were positioned as near as possible to the optical axis of each camera lens, routing the light from each strobe to illuminate the targets. This near on-axis lighting maximized the light return from the blade and ceiling retro-reflective targets. On average, there were

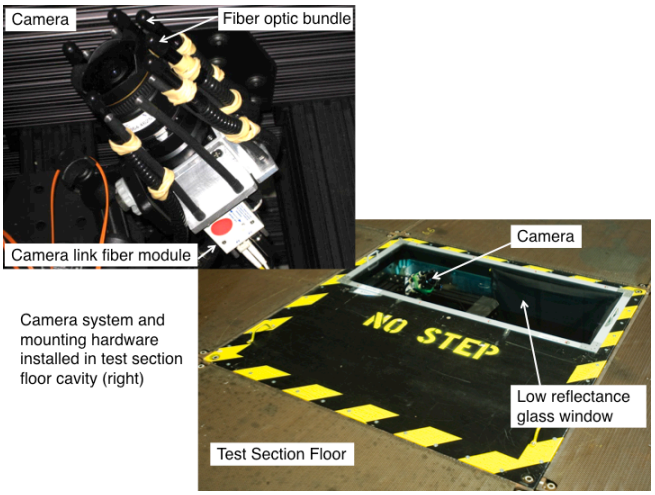

Figure 12. Camera installation inside test section floor viewport.

eight 0.25-inch diameter fiber optic bundles encompassing each camera lens to help distribute the emitted strobe light uniformly across the blades. Roughly 50% of the fiber bundles were capped with focusing lenses to further increase strobe illumination in areas of the rotor disk where the target light return was lower because of the highly oblique viewing angle.

Data Acquisition

The BD image acquisition hardware consisted of components in both the wind tunnel computer room and in the test section viewports. The data acquisition system consisted of four PC's running Windows XP Professional®, each with a Matrox Helios PCIX® frame grabber board that was interfaced via Camera Link® through fiber optic cables. Due to the extreme distances (> 250 ft) between the cameras and the BD data acquisition system, Camera Link fiber optic extender units, shown in Figure 12, were required to connect data via fiber from the cameras to the PC frame grabber boards. Acquisition software included NASA developed Rotor Azimuth Synchronization Program (RASP) rotor encoder (Ref. 16) and WingViewer image acquisition software (Ref. 17). A digital/delay pulse generator provided the synchronized trigger to the strobes and cameras based on the image acquisition software and RASP selection of azimuth. The master BD data acquisition system configuration, which enabled RASP to control the synchronized strobe, camera, and acquisition triggers to the other three systems, is illustrated in Fig. 13.

The strobes and cameras were triggered with the strobe light pulses occurring within the integration time of the CCD video cameras and with respect to the desired blade azimuth location in increments of 0.35° (degrees per shaft encoder count). All cameras and strobes were synchronized with the rotor shaft encoder to simultaneously capture the retro-reflective targets on the lower surface of each blade at an image-set acquisition rate of once per rotor revolution. Figure 14 illustrates a typical test section camera viewport installation and LRTA encoder signals.

Image data were taken for up to 60 consecutive revolutions to document the instantaneous and mean (via sample average) deformation of each blade at a specified rotor azimuth. This process was repeated for up to 40 rotor azimuth locations to document the deformation of each blade throughout the entire rotor disk. For the nominal rotor rotation rate of 258 RPM, one image per each of the eight cameras was captured every 0.23 seconds.

BD image data sets were categorized as either primary or secondary. For 28 of the 29 Airloads primary BD test conditions, images were acquired for 60 revolutions of data per azimuth, with eight cameras and 40 rotor azimuths, producing 19,200 individual images. (At one primary test condition, only 15 images were acquired at each azimuth for each camera.) The time required to acquire 60 images at each of the 40 rotor azimuths was approximately 14 seconds, leading to a total data acquisition time approaching 10 minutes. The data acquisition time proportionally increased during slowed rotor testing performed at 167 and 105 RPM. Secondary data sets consisted of 12 images per rotor azimuth that recorded a single blade per rotor quadrant for a data set of 11 azimuth positions over a range of 95°. Acquisition time for secondary data sets was approximately one minute. These secondary data sets were acquired during the majority of the Airloads wind tunnel test, during test conditions not identified as BD primary data sets. The highlighted test conditions in the Appendix are considered the primary BD conditions.

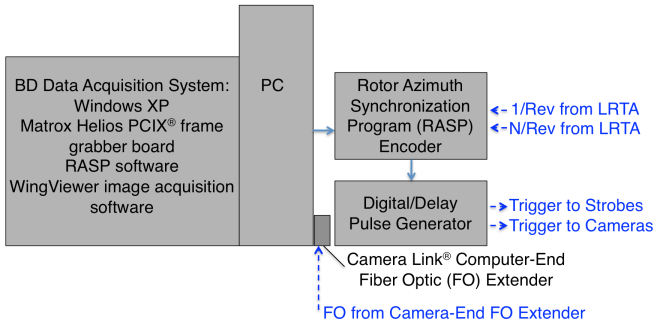

Figure 13. Master BD data acquisition system computer room components.

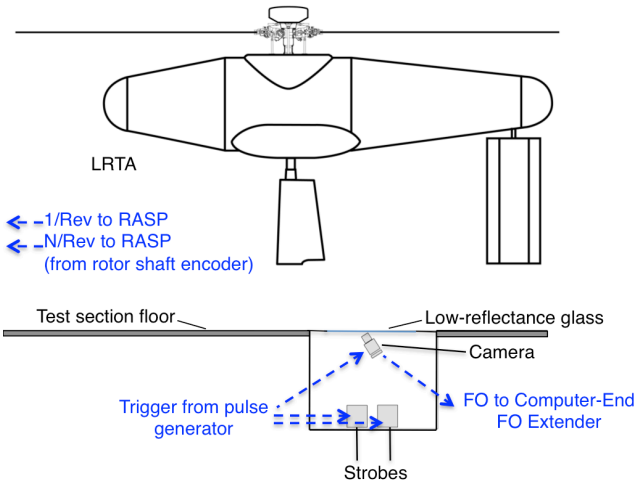

Figure 14. Test section installation of BD data acquisition components in camera viewport and LRTA encoder signals.

DATA ANALYSIS

Image Processing

Each set of images was digitally processed to calculate centroid locations of discrete targets on the rotor blades and test section ceiling. A suite of custom designed image processing and data reduction functions were developed using the Mathworks® Matlab software environment. Supporting functions for image processing, photogrammetry, and coordinate transformations are provided via a custom Matlab Photogrammetry Toolbox developed for NASA by

Western Michigan University (Ref. 18). This toolbox, in conjunction with the Matlab Image Processing and Statistics Toolboxes, were integrated into a NASA rotor-specific toolbox suite of functions. The NASA Rotor Toolbox makes use of moderately automated post-test image processing procedures that identify and calculate the image plane centroid spatial coordinates for each target. The Rotor Toolbox also contains a number of specialty scripts and functions for camera calibration, determining camera location and pointing angles, performing multi-camera intersections to determine 3D spatial coordinates for computing root pitch, flap, and lag angles as well as elastic deformations.

An interactive graphical user interface (GUI) is used for image processing of targets and target centroid inspections. The GUI provides some automation of the centroiding process, but manual inputs and visual inspection of images are required to detect and avoid potential image processing issues. A detailed description of the GUI is described in Ref. 9. Figure 15 shows an example of the blade centroid identification during the initial image processing step. After blade target numbering is properly identified and inspected using the first image of the sequence, the computation of target centroids for the second image thru the end of the image sequence is fully automated. Targets on the LRTA fuselage, test section ceiling, and instrumentation hat are useful visual guides during this processing step and visual inspection.

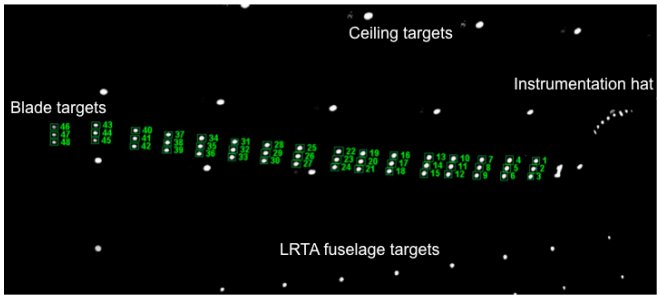

Figure 15. Example data image with the blade target numbers are outlined by green rectangles.

Centroid Validation

Centroid validation is necessary to confirm each identified blade target is visible in each image of the sequence. Although the first image of the data set is manually inspected, errors may exist due to the movement of the rotor blades about the image plane causing blocked targets in later images of the sequence. To avoid or correct partially blocked targets, centroid data for all images in a set must be inspected and validated. A separate centroid validation Matlab function was developed to assist with locating mislabeled or suspect centroid data that may require manual inspection and correction. For example, slowed-rotor, high advance ratio test conditions proved to be particularly challenging due to the extreme image-to-image blade motion (compared to lower advance ratios). Targets located in the line of sight near the LRTA fuselage can become partially blocked, causing the identified centroid locations to be offset. This holds true even near the inboard portion of the rotor blades. Figure 16 is an example where targets may appear in several images of a data set, but then disappear (either fully or partially) in later images of the same sequence. Figure 16a is a long-exposure close-up of the LRTA and inboard portion of the rotor blades with the blade area of interest indicated within the red box. Figures 16b and 16c are two data images from the same image sequence where the trailing edge targets of blade 1 can be seen in Fig. 16b, but are no longer visible in the next image, Fig. 16c. As the blade flaps, the LRTA fuselage

a. Close-up of LRTA with region of interest for Figs. 16b and 16c.

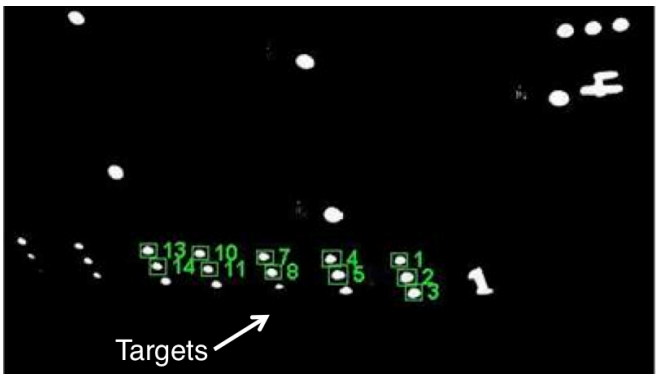

b. Trailing edge targets of Blade 1 are visible.

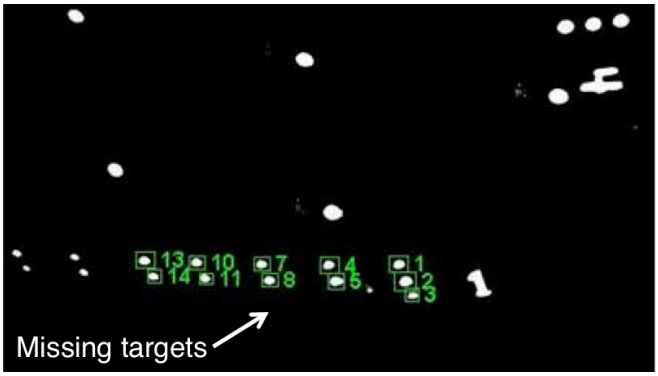

c. Trailing edge targets of Blade 1 become blocked by the LRTA fuselage.

Figure 16. Example of blade targets blocked by the LRTA fuselage for images from the same data sequence.

intermittently blocks the trailing edge targets. This is common for the inboard targets and caused difficulty in fully automating the image processing.

Another example of a centroid validation challenge is strobe reflections off of the camera viewport windows. Light from the xenon strobe, reflecting off the camera viewport window, can be seen in Figure 17. Although the reflection intensity has been reduced by a factor of approximately four by replacing the standard glass camera viewport windows with low-reflectance coated windows (Ref. 7), they continue to pose potential complications with image processing automation. The reflections generally affect only a few targets on each blade at a single blade azimuth position per camera (Fig. 17a). Consequently, rev-to-rev variations in blade position can cause the strobe reflections to intermittently merge with blade targets. Figure 17b illustrates two blade targets near the vicinity of a strobe reflection where the blade target is properly discriminated. However, in the same image sequence, the strobe reflection can merge with an adjacent target as indicated by the shaded red area of Fig. 17c, causing an error in the centroid location. More effective means for dealing with these occurrences would greatly improve the level of automation. Similar to strobe reflections, ceiling targets and ceiling lights also have the potential to interfere with blade targets.

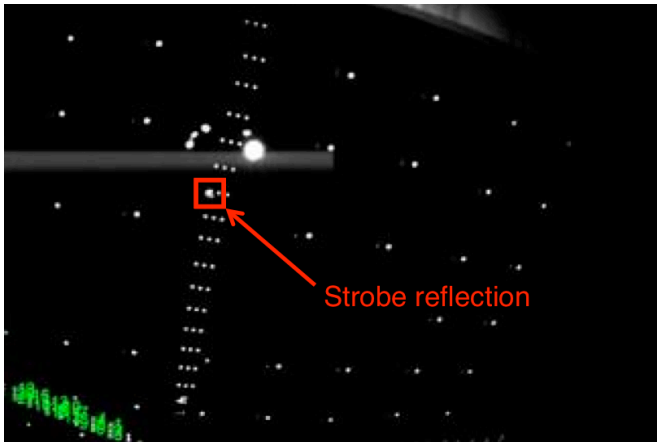

a. Typical image with strobe reflection near the vicinity of blade targets; Red box indicates area of interest for Figs. 17b and 17c.

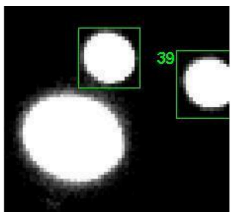

b. Image showing strobe reflection distinct from targets.

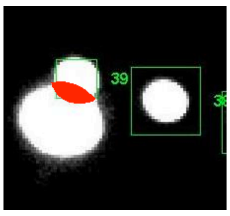

c. Image showing strobe reflection overlapping blade target; red region indicating combined grayscale.

Figure 17. Effect of strobe light reflection combining with target centroid.

Blade Position, Orientation and Deformation

The centroids are the 2D image coordinates of each target as seen by the cameras. If a target centroid is available for two or more cameras, then the target's 3D location in the wind tunnel coordinate system is determined via standard photogrammetry techniques (Ref. 14). The next step is to use these 3D locations to determine the blade orientation values of pitch, flap and lag for the azimuth obtained from the RASP system.

This is accomplished using a reference set of target locations, measured in the blade coordinate system, that were obtained while the blade was supported to minimize deformation, as shown in Fig. 9b. Details of how the reference locations were measured are given in Appendix H of Ref. 9. If the blades were perfectly rigid, then a series of geometric transformations representing pitch, flap, lag and azimuth could be applied to the reference target locations to produce the measured blade target locations for each data point. A nonlinear least squares process was used to find the best pitch, flap and lag values, for a given azimuth, that would transform the reference locations of the four inboard rows of targets to the measured locations for those targets each data point.

Due to elastic deformation of the measured blade at these inboard locations, this registration process can lead to errors in the estimated blade position and orientation with corresponding errors in the deformation values. This is illustrated in Fig. 18, which shows a hypothetical registration to estimate the flap angle. The green xz axes show the actual flap angle, β_{actual}, with the green line representing the deformed quarter-chord line of the measured blade. The dots along the line represent registration target rows. The blue xz axes show the estimated flap angle, $\beta_{estimated}$, that is found when fitting the reference target locations for the first four rows to the corresponding measured target locations. The difference in these two angles is the flap angle error due to blade elasticity. Similar errors occur for pitch and lag.

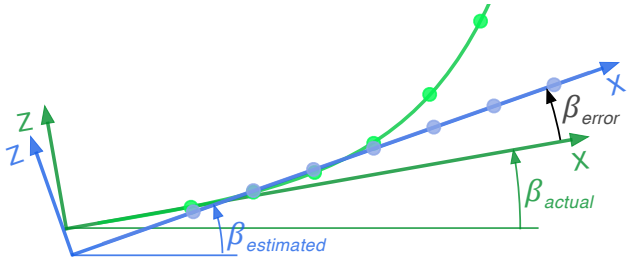

Figure 18. Illustration of flap angle estimate error due to blade elasticity.

Estimates of the errors were determined using curve fits through the inboard targets. These corrections are based on the following assumptions and procedures.

1) For the pitch angle correction, it is assumed that Δtwist is zero at the hinge point and that the first derivative of Δtwist with respect to X is also zero at the hinge point. The pitch angle correction is based on a cubic fit of the initial Δtwist estimates for the first three inboard rows. Application of pitch angle correction results in a zero value for Δtwist at the hinge point.

2) For the flap angle correction, it is assumed that ΔZ is zero at the hinge point and that the first and second derivatives of ΔZ with respect to X are also zero at the hinge point. The flap angle correction is based on a cubic fit of the ΔZ estimates for the first five inboard rows after the pitch angle correction has been applied. Both a flap angle correction and a ΔZ correction are determined. The ΔZ correction is determined and applied to enforce a zero value for ΔZ at the hinge point.

3) For the lag angle correction, it is assumed that ΔY is zero at the hinge point and that the first and second derivatives of ΔY with respect to X are also zero at the hinge point. The lag angle correction is based on a cubic fit of the ΔY estimates for the first five inboard rows after the pitch, flap and ΔZ corrections have been applied. Both a lag angle correction and a ΔY correction are determined. The ΔY correction is determined and applied to enforce a zero value for ΔY at the hinge point.

After these corrections were applied to the pitch, flap and lag angles, elastic deformations were then recalculated via comparison to the reference target coordinates.

RESULTS AND DISCUSSION

Preliminary blade displacement measurement results have been previously presented in several papers (Ref. 6-9). Those results are now superseded by the results presented in this paper and in Volume II of the final report (Ref 10). In general, the changes in blade root pitch, flap and lag between the prior, preliminary reports and the current results are not very significant. However, even small changes in estimated flap and pitch can lead to significant differences in the blade elasticity values ΔZ and Δtwist. (Values for elastic ΔX and ΔY were not included in any of the prior reports.) Examples of these changes are presented in Figures 19 and 20, which depict the uncorrected and corrected values for elastic ΔZ and Δtwist as a function of rotor radius for the test conditions originally included in Abrego, et al. (Ref. 7). These figures include the CFD/CSD predictions of elastic ΔZ and Δtwist presented in that paper. The "uncorrected" values for elastic ΔZ and Δtwist are very nearly the same as those presented in that paper, but are instead based on the most recent camera calibrations and data reduction procedures, excluding the registration error corrections. The "corrected" values include the registration error corrections.

Figure 19 shows estimated elastic ΔZ deformations from CFD/CSD predictions and from photogrammetry measurements at 0°, 150° and 255° blade-azimuth (ψ) locations for $\mu = 0.30$ and $C_T/\sigma = 0.10$. The "Uncorrected Measurement" values represented by green circles do not incorporate corrections to flap angle due to registration errors, which are included in the corrected values shown by the blue squares. The flap angle correction rotates the blade reference position, resulting in larger ΔZ corrections as the radial station increases. This is why the curve representing the corrected values looks somewhat like a rotation of the uncorrected curve. To give an idea of how different flap angle corrections would affect the ΔZ values, curves representing the ΔZ values for ±20% and ±50% deviations in the estimated flap angle correction are provided. For all three figures, the flap angle correction looks more realistic in that elastic ΔZ values asymptotically approach zero as r/R approaches zero. Figures 19a and 19c show much better agreement between the CFD/CSD predictions and the corrected measurement values out to an r/R of about 0.6.

While the agreement did not improve for Fig. 19b, it is clear that adjusting in the flap angle correction by −50%, it very nearly matches the CFD/CSD prediction. However, no adjustment of the flap angle correction would make the CFD/CSD predictions match the measured data for figures 19a and 19c over the entire span of the rotor. This would indicate that these CFD/CSD predictions are not fully capturing the spanwise elastic behavior at these azimuths.

Figure 20 shows estimated elastic Δtwist deformations from CFD/CSD predictions and from photogrammetry measurements for the same test conditions and blade azimuths as provided in figure 19. For elastic Δtwist deformations, the correction for the registration error due to blade deformation is a correction in the blade pitch angle, which simply shifts the elastic Δtwist values by an offset that is constant over the span of the rotor. Since it is easy to visualize how such offsets would affect the data, percentage variations in the value of the correction, as provided for in figure 19, are not provided. Elastic Δtwist estimates from the photogrammetric measurements have more uncertainty and show more scatter. This is primarily due to the angle measurements being essentially the derivative of measured target positions, whereas the ΔZ values are determined directly from measured target positions after blade orientation transformations are made. In Fig. 20a, the corrected Δtwist measurements for the first three radial stations fall right on top of the CFD/CSD prediction. However, the CFD/CSD prediction shows the Δtwist values becoming increasingly more negative as the radius increases, whereas the measured Δtwist values tend to level out. Changing the value of the correction used would not improve the comparison of the measured values to the CFD/CSD prediction. In Figs. 20b and 20c, a small change in the value of the pitch correction would make the measured Δtwist values better match the CFD/CSD predictions at the inboard stations. However, the CFD/CSD

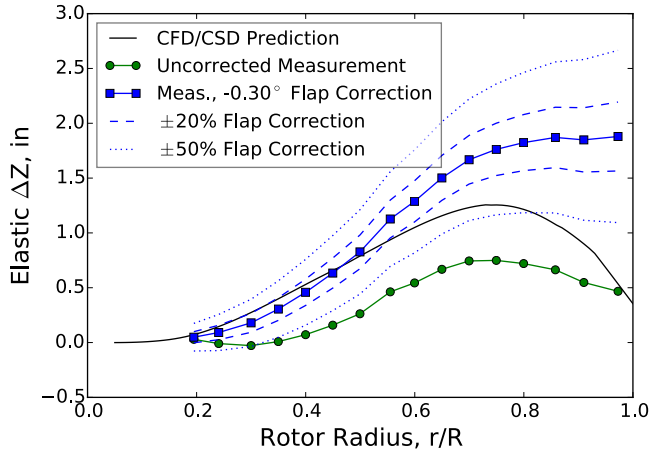

a. ψ = 0°

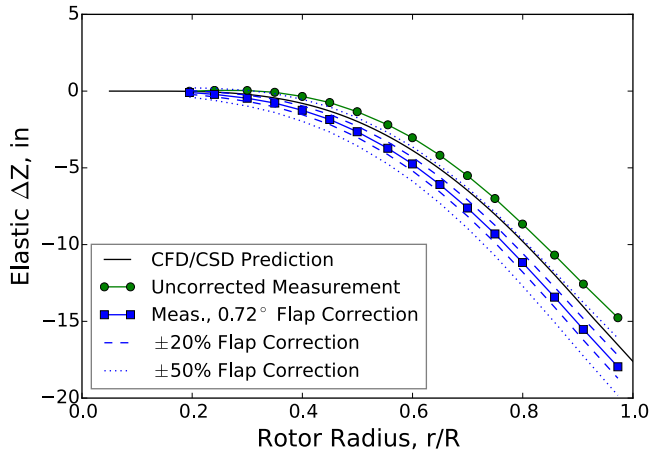

b. ψ = 150°

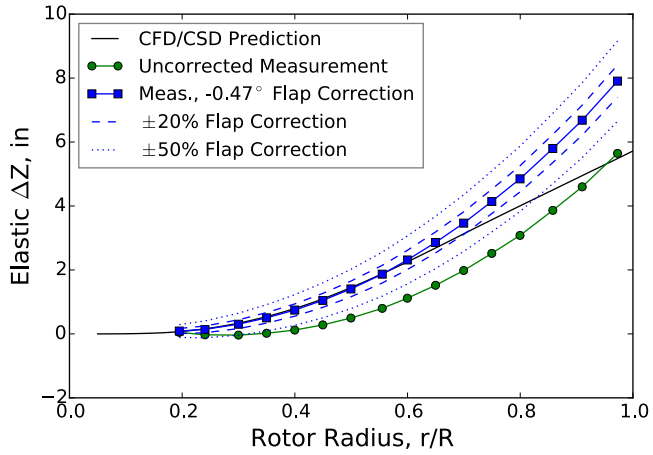

c. ψ = 255°

Figure 19. Estimated elastic ΔZ deformations from CFD/CSD and from corrected and uncorrected photogrammetry measurements at three blade-azimuth, ψ, locations for μ= 0.30 and CT/σ = 0.10.

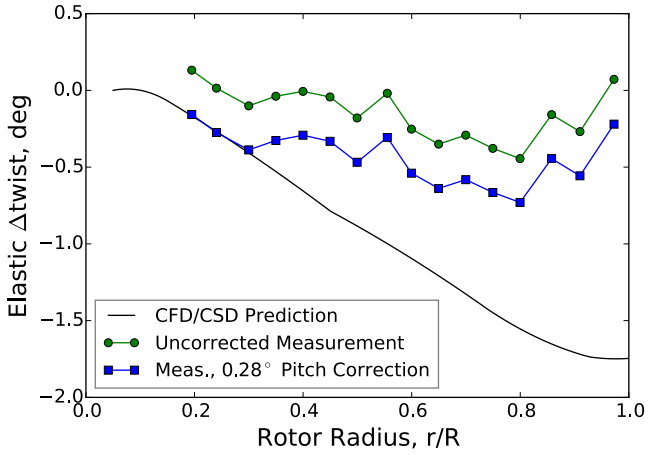

a. ψ = 0°

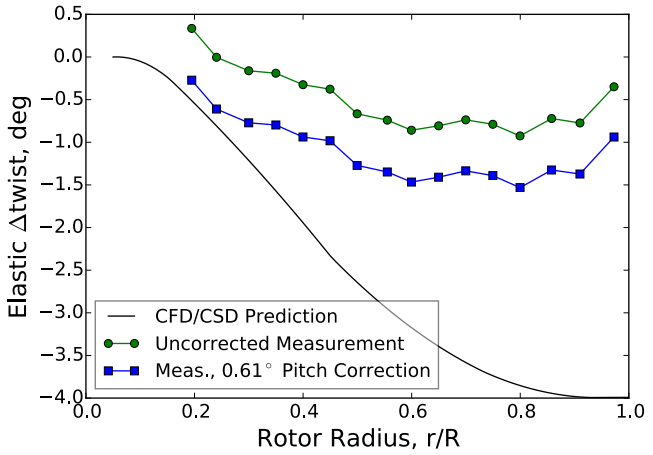

b. ψ = 150°

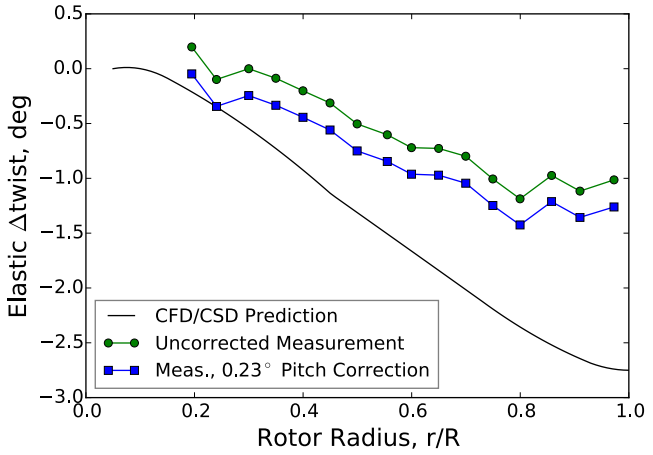

c. ψ = 255°

Figure 20. Estimated elastic Δtwist deformations from CFD/CSD and from corrected and uncorrected photogrammetry measurements at three blade-azimuth, ψ, locations for μ= 0.30 and CT/σ = 0.10.

predictions still show a strong trend of increasingly negative Δtwist values with radial station that is not shown by the measured values.

An extensive compilation of blade displacement measurement results is provided in the second volume of the final report (Ref. 10). The final report also contains plots and tables for all of the primary blade displacement data sets, for selected secondary data sets and for several reference data sets where the rotor was set to a common reference condition. The data and plots are derived from the latest camera calibrations and data reduction procedures. These include estimated corrections that account for registration errors due to blade bending.

Data Issues

While the BD team has high confidence in most of the final data set, there are a couple of caveats. First, the estimate lag angle values may have significant offset errors due to the potential that the rotor azimuth values used in data reduction may have had errors up to 2 degrees. This was initially suspected because the estimated lag values differed by up to 2 degrees from the lag measured using hub mounted instrumentation. Examination of targets on the instrumentation hat, as presented in Ref. 10, show run to run discrepancies of hat target locations for identical rotor azimuth values. This would indicate that there may be an issue with the value of the rotor azimuth used in reducing the data. The source of this discrepancy is not known, but it may be due to a time lag in either receiving the azimuth value from the wind tunnel data system or in triggering the photogrammetry data acquisitions. This may be correctable by using the hat targets to determine azimuth, but this process was not developed due to time and resource constraints.

The second caveat is that there are occasional data outliers. Some of these may be due to centroiding errors, but an effort was made to find and correct most of these. A second source of outliers in spanwise deformation data is when the data is determined from more than one set of camera combinations. Each camera calibration has bias errors, which leads to bias errors in target positions determined for each set of camera combinations. When the same set of cameras is used for all targets on a blade, they have a common bias error. This common bias error will affect pitch, flap and lag estimates, but should not affect the spanwise variation of elastic deformation estimates. However, if the inboard targets use one set of cameras and the outboard targets use a different set of cameras, the different bias errors for the two sets may cause a discontinuity in the spanwise distribution of estimated target positions, which results in a discontinuity in the spanwise variation of elastic deformation estimates. For most of the data presented, only one set of cameras was used for all targets on a blade for a specific azimuth and test condition. However, there are some cases where all the targets were not visible to each camera used, so more than one camera combination was used to get data for all of the visible targets. In these cases the differing bias errors can result in discontinuities in the spanwise variation of elastic deformation estimates.

CONCLUSIONS

Blade displacement measurements using multi-camera photogrammetry were acquired during the full-scale wind tunnel test of the UH-60A Airloads rotor, conducted in the NFAC 40- by 80-Foot Wind Tunnel. The primary objective of rotorcraft blade displacement measurements is to obtain accurate data for a range of relevant test conditions suitable for the validation of CFD/CSD methods capable of simulating full-scale flight conditions. The ability to photogrammetrically measure blade displacements, encompassing all blades throughout the full rotor azimuth at test conditions representative of actual free-flight has been successfully demonstrated.

The data and plots presented are derived from the latest camera calibrations and data reduction procedures. These include estimated corrections that account for registration errors due to blade elasticity. The changes in blade pitch, flap and lag between the previously reported results and the current results are small. However, even small changes in estimated flap and pitch can lead to significant differences in the blade elasticity values.

Estimated elastic ΔZ and Δtwist deformations from CFD/CSD predictions and from photogrammetry measurements at three blade-azimuth locations were presented. The flap angle correction rotates the blade reference position, resulting in larger ΔZ corrections as the radial station increases. For ΔZ deformations, the flap angle correction looks more realistic in that elastic ΔZ values asymptotically approach zero as r/R approaches zero. No adjustment of the flap angle correction would make the CFD/CSD predictions match the measured data completely. For elastic Δtwist deformations, the correction simply shifts the elastic Δtwist values by an offset that is constant over the span of the rotor. The corrected Δtwist measurements for the first three radial stations falls right on top of the CFD/CSD prediction. However, the CFD/CSD prediction shows the Δtwist values becoming increasingly more negative as the radius increases, whereas the measured Δtwist values tend to level out. In general, the data indicates that the CFD/CSD predictions are not fully capturing the spanwise elastic behavior.

While the BD team has high confidence in most of the data presented here, there are two caveats. The estimated lag angle values may have significant offset errors due to the potential that the rotor azimuth values used in the data reduction may have had errors up to 2 degrees. Second, occasional data outliers remain, possibly due to centroiding errors or when the data is determined from more than one set of camera combinations. In these cases the differing sets of

bias errors can result in discontinuities in the spanwise variation of elastic deformation estimates.

An extensive compilation of blade displacement measurement results is provided in the second volume of the final report (Ref. 10). The final report also contains plots and tables for all of the primary blade displacement data sets, for selected secondary data sets and for several reference data sets where the rotor was set to a common reference condition.

Author contact: Anita Abrego Anita.I.Abrego@nasa.gov
Larry Meyn Larry.Meyn@nasa.gov, Alpheus Burner
Alpheus.W.Burner@nasa.gov

ACKNOWLEDGMENTS

The authors thankfully recognize the efforts and significant contributions made during the planning, development, and implementation of the blade displacement measurements for UH-60A Airloads Wind Tunnel Test. Acknowledgement is made to Thomas Norman, Gloria Yamauchi, Alan Wadcock (NASA Ames), and Gary Fleming (NASA LaRC) for their early involvement with the BD measurement effort. Gary Fleming also developed and provided assistance with the rotor azimuth synchronization program (RASP). Edward Massey (Jacobs Technology-NASA LaRC) is acknowledged for his modifications to the WingViewer image acquisition software to accommodate special requirements for rotor testing. Further acknowledgement is extended to Susan Gorton, Luther Jenkins and Odilyn Santamaria-Luck (NASA LaRC) for program leadership and to Harriett Dismond, Benny Lunsford, Kelvin Santiago, Felecia Berry, Kristina Chapman, Lisa Le Vie, Karlus Grant, Jack Woodward (NASA LaRC), Eduardo Solis, Charles Rogers, Michael Henderson, Benny Cheung, and Dan Christensen (NASA Ames), along with the entire NFAC test team for their strong support of the BD effort.

In addition Thomas Jones (NASA LaRC) is acknowledged for technical advice in camera self-calibration and for calibrations of four of the cameras. Professors Stuart Robson (University College London) and Mark Shortis (RMIT University, Melbourne, Australia) are acknowledged for consultation on the distortion of fish-eye lenses and alternate methods of lens correction.

Finally, we wish to acknowledge and thank retiree Larry Olson for his dedication, hard work, and innovations with the Blade Displacement Measurement effort. We wish him the very best in his retirement.

REFERENCES

[1]Norman, T. R., Shinoda, P., Peterson, R. L., Datta, A., "Full-Scale Wind Tunnel Test of the UH-60A Airloads Rotor," American Helicopter Society 67th Annual Forum, Virginia Beach, VA, May 2011.

[2]Kufeld, R. M., Balough, D. L., Cross, J. L., Studebaker, K. F., Jennison, C. D. and Bousman, W. G., "Flight Testing of the UH-60A Airloads Aircraft," American Helicopter Society 50th Annual Forum, Washington D.C., May 1994.

[3]Jenkins, L. N., Barrows, D. A., Cheung, B. K., Lau, B. H., Okojie, R. S., Wadcock, A. J., Watkins, A. N., Yao, C. S., "Chapter 5 – Experimental Capabilities, A Status of NASA Rotorcraft Research", edited by Gloria K. Yamauchi and Larry A. Young, NASA TP-2009-215369, September 2009.

[4]Schneider, Oliver, and van der Wall, Berend G., "Final Analysis of HART II Blade Deflection Measurement," 29th European Rotorcraft Forum, Friedrichshafen, Germany, September 16-18, 2003.

[5]Olson, L. E., Barrows, D. A., Abrego, A. I. and Burner, A. W., "Blade Deflection Measurements of a Full-Scale UH-60A Rotor System," 2010 AHS Specialists' Conference on Aeromechanics, San Francisco, CA, January 20-22, 2010.

[6]Barrows, D. A., Burner, A. W., Olson, L. E., and Abrego, A. I., "Blade Displacement Measurements of the Full-Scale UH-60A Airloads Rotor", 2011 AIAA Applied Aerodynamics Conference, Honolulu, Hi, June 27-30, 2011.

[7]Abrego, A. I., Olson, L. E., Romander, E. A., Barrows, D. A., Burner, A. W., "Blade Displacement Measurement Technique Applied to a Full-Scale Rotor Test", 2012 AHS 68th Annual Forum, Fort Worth, Tx, May 1-3, 2012.

[8]Romander, E., Meyn, L., Norman, T. R., Barrows, D., Burner, A., A., "Blade Motion Correlation for the Full-Scale UH-60A Airloads Rotor," Fifth Decennial AHS Aeromechanics Specialists' Conference, San Francisco, CA, Jan 2014.

[9]Biedron, R. T., Lee-Rausch, E. M., "Blade Displacement Predictions for the Full-Scale UH-60A Airloads Rotor", 2014 AHS 70th Annual Forum, Montreal, Quebec, May 20-22, 2014.

[10]Meyn, L., Abrego, A., Barrows, D., Burner, A., "Blade Displacement Measurements During the NFAC UH-60A Airloads Test," NASA TM, NASA Ames Research Center, December 2015 (to be published).

[11]Norman, T. R., Shinoda, P. M., Kitaplioglu, S. A., Jacklin, S. A. and Sheikman, A., "Low-Speed Wind Tunnel Investigation of a Full-Scale UH-60 Rotor System,"

American Helicopter Society 58th Annual Forum, Montreal, Canada, June 2002.

[12]Luhmann, T., Robson, S., Kyle, S., and Harley, I., *Close Range Photogrammetry: Principles, Techniques and Applications*, John Wiley & Sons, 2006.

[13]Burner, A. W. and Liu, T., Videogrammetric Model Deformation Measurement Technique. AIAA J. of Aircraft, vol. 28, no. 4, July-August, 2001, pp. 745-754.

[14]Barrows, D., "Videogrammetric Model Deformation Measurement Technique for Wind Tunnel Applications," 45th AIAA Aerospace Sciences Meeting and Exhibit, American Institute of Aeronautics and Astronautics, Jan 8-11 2007.

[15]Geodetic Systems, Inc., V-STARS, http://www.geodetic.com/.

[16]Fleming, G. A., "RASP: Rotor Azimuth Synchronization Program (RASP) User's Guide, Version 1.3," Tech. Rep., NASA Langley Research Center, February 6 2008.

[17]Amer, T. R. and Goad, W. K., "WingViewer: Data Acquisition Software for PSP/TSP Wind Tunnel Cameras," Tech. Rep. LAR-16474-1, NASA Langley Research Center, October 2005.

[18]Liu, T. and Burner, A. W., "Photogrammetry Toolbox Reference Manual," NASA/CR 2014-218518, NASA Langley Research Center, Hampton, VA, September 2014.

APPENDIX

The following tables present the UH-60A Airloads wind tunnel test conditions with blade displacement primary conditions highlighted in bold.

Parametric Sweep Test Conditions

M_{tip}	α_s	μ	C_T/σ
0.650	-8	0.30	0.02 to 0.12
		0.35	0.02 to 0.11
		0.37	0.02 to 0.11
	-4	**0.15**	**0.08**
		0.24	0.02 to 0.126
		0.30	0.02 to 0.118
		0.35	0.02 to 0.11
	0	**0.15**	0.04 to 0.13 **(0.08)**
		0.20	0.04 to 0.13
		0.24	0.02 to 0.127 **(0.13)**
		0.30	0.02 to 0.124 **(0.10)**
		0.35	0.02 to 0.11
	4	**0.15**	0.06 to 0.13 **(0.08)**
		0.20	0.02 to 0.12
		0.24	0.02 to 0.12
		0.30	0.06 to 0.08 **(0.08)**
	8	**0.15**	0.06 to 0.12 **(0.08)**
		0.20	0.06 to 0.12
		0.24	0.06 to 0.12
		0.30	**0.08**
0.625	0	0.24	0.02 to 0.131
		0.30	0.02 to 0.125
0.675	-8	0.35	0.02 to 0.10
		0.37	0.02 to 0.10
		0.385	0.02 to 0.09

1-g Level Flight Test Conditions

C_L/σ	μ	M_{tip}
0.08	**0.15**, 0.20, 0.24, 0.30, **0.35**, **0.37**, 0.385, **0.40**	**0.650**
0.09	0.15, 0.20, 0.24, 0.30, 0.35, 0.37, 0.385, 0.40	0.650
0.10	0.15, 0.20, 0.24, 0.30, 0.35, 0.37, 0.385	0.650

Flight/DNW Test Simulation Conditions

Test	Test Pt #	M_{tip}	μ	C_T/σ
Flight	**C8424**	**0.638**	**0.30**	**0.087**
	C8525	0.643	0.23	0.077
	C9020	**0.669**	**0.245**	**0.118**
DNW	**11.24**	**0.629**	**0.30**	**0.10**
	13.12	**0.638**	**0.30**	**0.07**
	13.20	**0.637**	**0.15**	**0.07**

Slowed Rotor Test Conditions

M_{tip}	α_s	μ	θ_0
0.650	0	0.30	0, 2, 3, 4, 6, 8, 10
		0.40	0.5, 2, 3, 4, 6, 8
	2	0.30	0, 2, 3, 4, 6, 8, 10
		0.40	0, 2, 3, 4, 6, 8
	4	0.30	0, 2, 3, 4, 6
		0.40	0, 2, 3, 4, 6
0.420	**0**	0.30	0, 2, 3, 4, 6, 8
		0.40	0, 2, 3, 4, 6, 8
		0.50	0, 2, 3, 4, 6, 8
		0.60	**0**, 2, 3, 4, 6, 8
0.260	**0**	0.30	0, 2, 3, 4, 6, 8
		0.40	0, 2, 3, 4, 6, 8
		0.50	0, 2, 3, 4, 6, 8
		0.60	**0**, 2, 3, 4, 6, 8
		0.70	0, 2, 3, 4, 6, 8
		0.80	0, 2, 3, 4, 6, 8
		0.90	0, 2, 3, 4
		1.00	**0**, 1, 2
	2	0.30	2
		0.40	2
		0.50	2
		0.60	**2**
		0.70	2
		0.80	2
		0.90	2
		1.00	**1**
	4	0.30	0, 2, 3, 4, 6, 8
		0.40	0, 2, 3, 4, 6, 8
		0.50	0, 2, 3, 4, 6, 8
		0.60	**0**, 2, 3, 4, 6, 8
		0.70	0, 2, 3, 4, 6, 8
		0.80	0, 2, 3, 4, 6, 8
		0.90	0, 2, 3, 6
		1.00	**0**, 2

PIV Test Conditions

M_{tip}	α_s	μ	C_T/σ	Azimuth delay
0.65	0	0.15	0.08	5, 15, 30, 45, 60, 75, 95, 135, 185, 225, 275, 315
0.65	4	0.15	0.08	5, 15, 30, 45, 60, 75, 95, 135, 185, 225, 275, 315
0.638	-4.82	0.30	0.087	5, 15, 30, 45, 60, 75, 95
0.65	0	0.24	0.07, 0.09	5
0.65	**0**	**0.24**	**0.11**	**5, 15, 30, 45, 60, 75, 95, 185, 275**
0.65	0	0.15	0.07, 0.09, 0.11, 0.12	15
0.65	**-6.9**	**0.35**	**0.08**	**5, 10, 15, 20, 30, 45, 60, 75, 95, 185, 275**